Analysis and Design of a Small-ScaleWingtip-Mounted Pusher Propeller

Stokkermans, Tom; Nootebos, Bas; Veldhuis, Leo

DOI
10.2514/6.2019-3693

Publication date
2019

Document Version
Final published version

Published in
AIAA Aviation 2019 Forum

AIAA AVIATION Forum
17-21 June 2019, Dallas, Texas
AIAA Aviation 2019 Forum

10.2514/6.2019-3693

Analysis and Design of a Small-Scale Wingtip-Mounted Pusher Propeller

Tom C. A. Stokkermans*, Sebastiaan Nootebos† and Leo L. M. Veldhuis‡
Delft University of Technology, 2629 HS Delft, The Netherlands

The wingtip-mounted pusher propeller, which experiences a performance benefit from the interaction with the wingtip flowfield, is an interesting concept for distributed propulsion. This paper examines a propeller design framework and provides verification with RANS CFD simulations by analysing the wing of a 9-passenger commuter airplane with a wingtip-mounted propeller in pusher configuration. In the taken approach, a wingtip flowfield is extracted from a CFD simulation, circumferentially averaged and provided to a lower order propeller analysis and optimisation routine. Possible propulsive efficiency gains for the propeller due to installation are significant, up to 16% increase at low thrust levels, decreasing to approximately 7.5% at the highest thrust level, for a range of thrust from 5% up to 100% of the wing drag. These gains are found to be independent of propeller radius for thrust levels larger than 30% of the wing drag. Effectively, the propeller geometry is optimized for the required thrust and to a lesser degree for the non-uniformity in the flowfield. Propeller blade optimization and installation result in higher profile efficiency in the blade root sections and a more inboard thrust distribution.

Nomenclature

b	=	Wing span, m
C_D	=	Drag coefficient
C_L	=	Lift coefficient
C_p	=	$(p - p_\infty)/q_\infty$ pressure coefficient
C_Q	=	$Q/\left(\rho_\infty n^2 D_\mathrm{p}^5\right)$ torque coefficient
C_T	=	$T/\left(\rho_\infty n^2 D_\mathrm{p}^4\right)$ thrust coefficient
c	=	Chord, m
D_p	=	Propeller diameter, m
D	=	Wing drag, N
h_i	=	Average cell size of grid i, m
J	=	$V_\infty/(nD_\mathrm{p})$ advance ratio
L	=	Wing lift, N
n	=	Propeller rotational speed, s^{-1}
P	=	Shaft power, W
p	=	Static pressure, Pa
Q	=	Torque, Nm
Q'	=	Torque distribution, $\mathrm{Nm} \cdot \mathrm{m}^{-1}$
q	=	Dynamic pressure, Pa
R_p	=	Propeller radius, m
$R_{\mathrm{p,ref}}$	=	Reference XPROP propeller radius, m
r	=	Radial coordinate in propeller reference frame, m
T	=	Thrust, N
T'	=	Thrust distribution, $\mathrm{N} \cdot \mathrm{m}^{-1}$
U_s^*	=	Standard deviation of a fit based on theoretic order of convergence
U_ϕ	=	Estimated discretization uncertainty
V	=	Velocity, $\mathrm{m} \cdot \mathrm{s}^{-1}$
x	=	Axial coordinate, m
y	=	Vertical coordinate, m
y^+	=	Dimensionless wall distance
z	=	Lateral coordinate, m
α	=	Angle of attack, deg
β	=	Blade pitch angle, deg
η_p	=	TV_∞/P propeller propulsive efficiency
ρ	=	Density, $\mathrm{kg} \cdot \mathrm{m}^{-3}$
φ	=	Propeller blade phase angle, deg
ϕ_i	=	Numerical solution obtained using grid i
ω	=	Vorticity, s^{-1}

Subscripts

0	=	Extrapolated
$0.7R_\mathrm{p}$	=	Radial coordinate, in which r/R_p is equal to 0.7
a	=	Axial
c	=	Chord based
iso	=	In isolated condition
h	=	Hub
k	=	Kink
p	=	Propeller
r	=	Root
t	=	Tangential, tip
∞	=	Freestream

*Ph.D. Candidate, Flight Performance and Propulsion Section, Faculty of Aerospace Engineering, AIAA Member, t.c.a.stokkermans@tudelft.nl.
†M.Sc. Graduate, Flight Performance and Propulsion Section, Faculty of Aerospace Engineering
‡Full Professor, Head of Flight Performance and Propulsion Section, Faculty of Aerospace Engineering, AIAA Member.

I. Introduction

Today's research on propellers is driven by their potential for reduced fuel consumption compared to turbofan propulsion. Not only the high propulsive efficiency of the propeller itself, but also its location on the airframe can enhance the overall efficiency of the aircraft. Wingtip-mounted propellers have been envisaged for their favorable interaction effects. For the tractor propeller variant, the interaction of the wing with the slipstream results in a reduction of the wing induced drag if the rotation direction of the propeller is opposite to that of the wingtip vortex [1–3]. The pusher propeller variant experiences a reduction in shaft power due to the swirling vortex inflow from the wingtip in case the propeller rotates against the direction of the wingtip vortex [2, 4–6]. Moreover, the modification of the wingtip vortex may reduce wing induced drag as well. Yet, the ingestion of the non-uniform inflow field may result in a noise penalty for the pusher variant. Adverse aeroelastic effects due to the large weight of an engine at the tip of a wing and the large yawing moment arm of the thrust vector in case of a one-engine-inoperative condition have prevented the application of wingtip-mounted propellers up to now. However, the emergence of electric propulsion in aircraft allows almost penalty-free downscaling of the propeller due to the scale independence of the electric motor [7]. This makes it possible to distribute the propulsion for instance through a hybrid-electric architecture, and enables to scale down the wingtip-mounted propeller like proposed in the SCEPTOR concept [8].

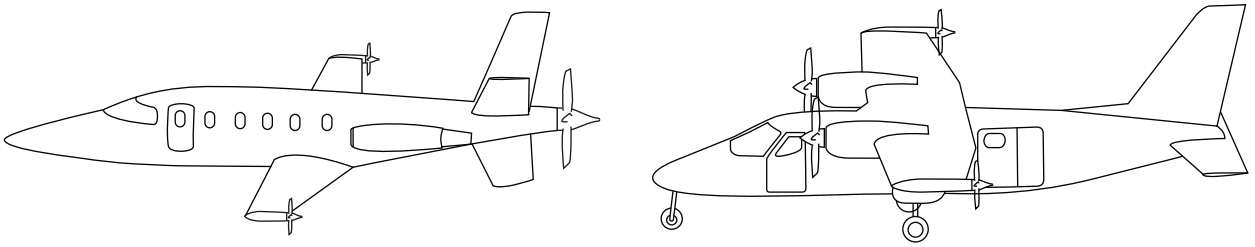

a) Modified Learfan 2100 **b) Modified Tecnam P2012 Traveller**

Fig. 1 Impression of airplane concepts with small-scale wingtip-mounted pusher propellers.

In this research the pusher variant is investigated in the context of distributed propulsion. An impression of such a concept, combining i.e. fuselage boundary layer ingestion and wingtip-mounted pusher propellers through a hybrid electric architecture, is shown in Fig. 1 a. A more conventional airplane layout with small-scale wingtip-mounted pusher propellers is sketched in Fig. 1 b. The design freedom to scale propellers and to distribute propulsion, results in a non-unique thrust requirement. For example, the propeller can be designed to balance just the induced drag of the wing or balance the entire cruise drag of the aircraft. The resulting performance benefit of propeller installation at the wingtip may depend on the thrust level. Hence the following research question: How does propeller scale influence the propulsive efficiency benefit and the upstream aerodynamic loading on the wing? Up to now, only research on a full scale wingtip-mounted pusher propeller has been performed, with a propeller not specifically designed for this task [4]. The inflow to the propeller is non-uniform, especially when the propeller becomes smaller relative to the wingtip flowfield. For a boundary layer ingestion propeller, Ref. [9] has shown that maximizing the propulsive efficiency gain requires a different design to cope with the non-uniform inflow experienced on the aft fuselage. Analogue to that, the wingtip-mounted pusher propeller may also benefit from design optimization, resulting in the second research question: To what extent can the propulsive efficiency benefit be increased by designing the propeller for the non-uniform inflow experienced at the wingtip?

This research, which is regarded as an extension of Ref. [10], gives insight in these questions by analysis of a specific case through the following steps:

1) CFD analyses of the wing are performed in order to quantify the wing performance and extract the wingtip flowfield.
2) A lower order propeller analysis and optimisation routine PROPR is established and validated for uniform inflow.
3) The wingtip flowfield is fed to PROPR for analysis and design optimization.
4) The upstream effect of the propeller designs on the wing performance is analyzed through CFD analyses of the wing with an actuator disk representation of the propeller.
5) The accuracy of PROPR for the non-uniform wingtip flowfield is checked through a fully resolved propeller–wing CFD simulation.

II. Computational Methods

A. RANS CFD Simulations

Four different types of RANS CFD simulations were performed in order to establish the wing performance and wingtip flowfield, to estimate the upstream effect of the propeller on the wing and to verify the accuracy of PROPR:

- Isolated wing simulations
- Isolated propeller simulations
- Wing simulations with actuator disk propeller representation
- A propeller–wing simulation

The wing used for these simulations was derived from the Tecnam P2012 Traveller [11], a twin-prop 9-passenger commuter airplane with a maximum take-off mass of 3600 kg. Only the wing was taken into account, without the original propeller and nacelles. A sketch of the wing is shown in Fig. 2 a. A minimum radius nacelle was added at the tip of the wing, extending aft of the trailing edge to accommodate a propeller in pusher configuration. The nacelle radius was kept equal to the propeller hub radius R_h. Hence, so far there is no provision to accommodate an electric motor. The wing parameters are given in Table 1 and are partly based on Ref. [12].

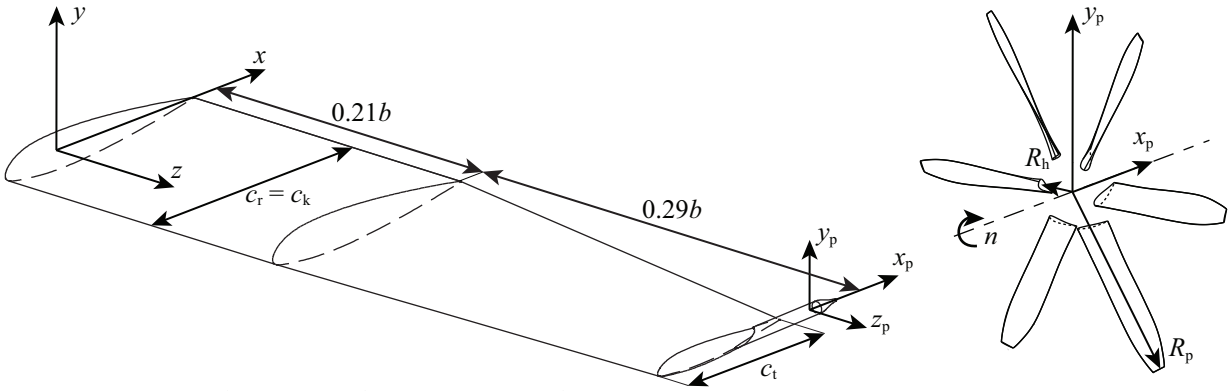

a) Wing model with nacelle and spinner. **b) XPROP propeller model.**

Fig. 2 Isometric view of the wing and TU Delft research propeller XPROP.

The propeller in the isolated propeller and propeller–wing simulations is the 6-bladed XPROP propeller, shown in Fig. 2 b, a research propeller from Delft University of Technology typical for turboprop airplanes. An extensive grid study and experimental validation for this propeller was performed in Ref. [13], and the same propeller grid density was used in this research. The spinner was modified to convert it into a pusher propeller. The propeller was used in its original size with a radius of $R_{p,ref} = 0.2032$ m and hub radius of $R_h = 0.23R_{p,ref}$. Simulations were also performed with proportionally scaled versions of smaller and larger size.

Table 1 Wing model parameters.

Parameter	Value
Span b	13.55 m
Root and kink chord c_r, c_k	2.06 m
Tip chord c_t	1.38 m
$c/4$ sweep, dihedral, twist	0°
Root and kink airfoil	NACA23015
Tip airfoil	NACA23012
Cruise speed	80 m/s
Cruise altitude	3048 m
Cruise angle of attack	3°
Cruise lift coefficient	≈ 0.35

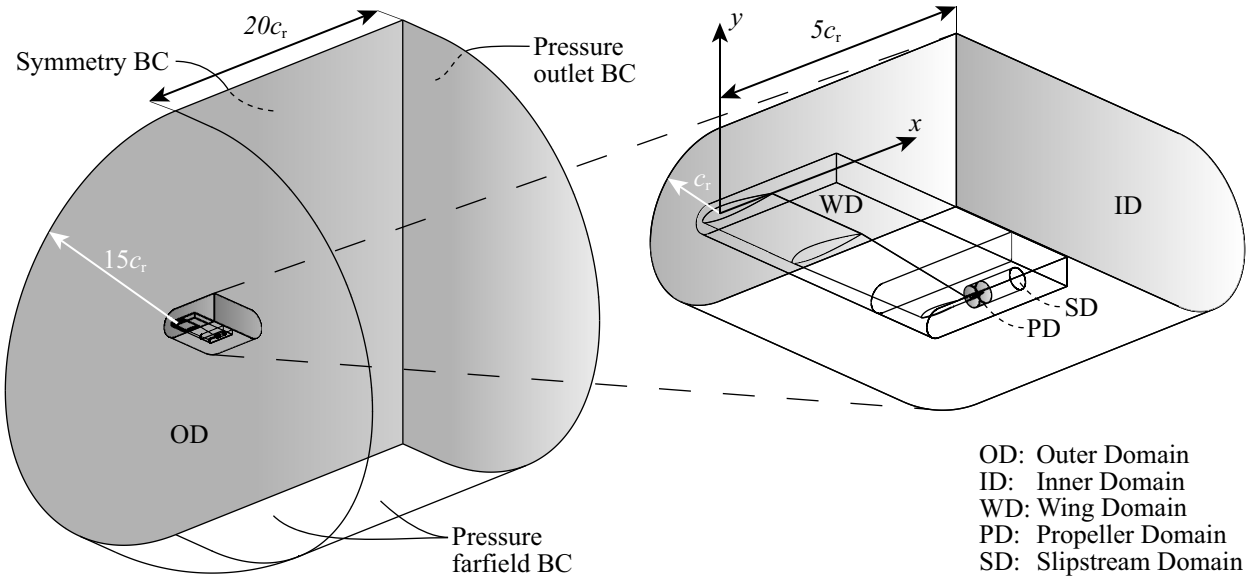

Fig. 3 Computational domain and boundary conditions for the wing simulations.

The RANS equations for compressible flow were used with a 2nd order accurate scheme in ANSYS® Fluent 18.1 [14], a commercial, unstructured, finite volume, cell-centered solver. For the propeller–wing simulations time-dependent solutions were found by a 2nd order backward Euler scheme with a time step equivalent to 2 deg of propeller rotation. Discretization of the advection term was done with an upwind scheme using the Barth–Jesperson boundedness principle [15]. For the equation of state, an ideal gas was assumed and Sutherland's law was used to predict the corresponding dynamic viscosity. Standard atmospheric conditions at the cruise altitude were assumed. The turbulence model was selected based on the findings of Kim and Rhee [16], who tested several turbulence models to simulate the wingtip vortex of an isolated wing. The eddy viscosity model in their research that best agreed with experimental data in terms of static pressure and axial velocity in the wingtip-vortex core was the Spalart–Allmaras (SA) one-equation model [17] with modification proposed by Dacles-Mariani et al. [18] to prevent build-up of turbulence viscosity in vortex cores. Therefore, this model was selected for the current research. Values for the inlet turbulence quantities were based on the recommendations by Spalart and Rumsey [19], which resulted in an eddy viscosity ratio of 0.21044 for the SA model. In order to fully resolve the boundary layer, the y^+ value on the no-slip walls of the model was less than one.

The computational domain and boundary conditions for the wing simulations are shown in Fig. 3. The outer dimensions of the domain were chosen to be sufficiently large with respect to the wing chord, in order to minimize the influence of the boundary conditions on the flow properties near the wing. At the domain inlet, a total-pressure jump with respect to the undisturbed static pressure was set to reach the cruise speed. Furthermore, the undisturbed total temperature was specified. At the domain outlet, the static pressure was prescribed to be on average equal to undisturbed static pressure. On the outboard side of the domain, a Riemann-invariant pressure farfield condition was specified with a Mach number, static pressure and static temperature complying with the inlet conditions. On the inboard side side, a symmetry boundary condition was imposed. The wing, nacelle, propeller and spinner were modeled as no-slip walls. The computational domain was divided in several domains for refinement of the grid. The propeller domain (PD) was connected to the other domains through sliding mesh interfaces to allow grid rotation for simulation of propeller motion. This domain could be replaced by a domain without propeller blades for the isolated wing simulations and wing simulations with actuator disk representation of the propeller. The actuator disk model described in Ref. [20] was used, requiring the propeller blade radial distribution of thrust and torque as input. Grids were constructed by means of ANSYS® Meshing. For regions adjacent to no-slip walls, the unstructured grid was made up of a triangular wall mesh, followed by layers of semi-structured prismatic elements of the inflation layer. For the remainder of the domain tetrahedral elements were used. Grid density in the whole domain was controlled by wall refinement of all no-slip walls, volume refinement of the domains, a 1st layer thickness of the inflation layers, and growth rates of the inflation layers and the remainder of the grid. Grid study results for the isolated wing are shown in Section III.

The computational domain and boundary conditions for the isolated propeller simulations are described in Ref. [13]. Since the wake of a propeller with axisymmetric nacelle is cyclic with the number of the blades, only a single blade was modeled in a wedge shaped domain with appropriate boundary conditions. The movement of the propeller and spinner was simulated with a rotating reference frame.

B. Propeller Analysis and Optimisation Routine: PROPR

To perform quick propeller analyses and to aerodynamically design the propeller for optimized performance, a PRopeller analysis and OPtimisation Routine named *PROPR* was set up based on XROTOR [21]. The software program uses discrete line vortices forming a semi-rigid wake to iteratively determine the induced velocities and has been used before by Refs. [9, 22–25] for both uniform and non-uniform inflow. XFOIL [26] was selected for airfoil analyses. All details of PROPR are described in Ref. [10]. Twenty radial sections were used to define the propeller geometry and provide XROTOR with airfoil data. Each radial section was supplied with the correct non-uniform flowfield. Fully turbulent flow for the airfoil data was assumed to allow comparison with the fully turbulent CFD simulations and to increase stability of running XFOIL in an optimization framework. The non-linear part of the lift curve was modified using an empirical model by Snel et al. [27] to correct two dimensional data for three dimensional rotational effects. Comparison of PROPR results with validation data is provided in Section IV.

III. Isolated Wing Analysis

CFD analyses of the wing were performed at 3 deg angle of attack to represent a cruise condition. A grid dependency study was performed to estimate the discretization uncertainty and to select an appropriate grid density. All refinements were varied systematically, except for the inflation layer, which was kept constant in line with Roache [28]. To estimate discretization uncertainty, the least-squares version of the grid convergence index (GCI) proposed by Eça and Hoekstra [29] was applied, with the alteration of using only the theoretical order of the solver of 2 to estimate the extrapolated grid results. Table 2 gives an overview of the grid sizes and wing lift and drag found for each grid. Table 3 presents the extrapolated lift and drag ϕ_0, the standard deviation of the fit based on the theoretical order of convergence U_s^* and the estimated discretization uncertainty U_ϕ for grid 2. The uncertainty of 0.49% and 3.10% for the lift and drag coefficient respectively was deemed acceptable for this study.

Table 2 Overview of grids and resulting isolated wing performance.

Grid	No. of cells	h_i/h_1	C_L [-]	C_D [-]
4	8,561,478	1.82	0.3434	0.01638
3	16,315,794	1.47	0.3440	0.01622
2	32,756,863	1.16	0.3447	0.01600
1	51,424,220	1.00	0.3452	0.01585

Table 3 Grid extrapolation results and estimated discretization uncertainties for grid 2.

	C_L	C_D
ϕ_0	0.3458	0.01568
U_s^* (%)	0.08	0.57
U_ϕ (%)	0.49	3.10

From the solution on grid 2 the flowfield that was fed to PROPR was extracted from the propeller plane, the plane where the propeller will be installed. The flowfield at the wingtip is visualised in Fig. 4 by means of streamtraces and the wingtip vortex is shown by an axial vorticity isosurface. On the isosurface and the propeller plane the velocity magnitude is plotted and on the wing surface the pressure coefficient distribution is shown. In Fig. 5 this flowfield at the propeller plane is given for the left wingtip as seen from behind, by means of contour plots of the axial and tangential velocity components. These velocity components are most relevant for the propeller aerodynamic loading and, together with the propeller rotational speed and propeller induced velocities, determine the local blade section angle of attack and dynamic pressure. The tangential velocity component is defined positive in the rotation direction of the propeller, which is running counterclockwise for the left propeller when seen from behind. In PROPR, the inflow flowfield is radially varying but assumed to be circumferentially constant. Therefore a circumferential average of this flowfield was taken, which will impact the resulting propeller response as follows: In the axial velocity contour plot the reduced velocity in the wake of the wing is clearly visible and its effect on the propeller will be averaged. In the tangential velocity plot a region of strong negative velocity and a region of positive velocity can be observed which have an opposite effect on the propeller. These regions will also be circumferentially averaged in a net negative velocity.

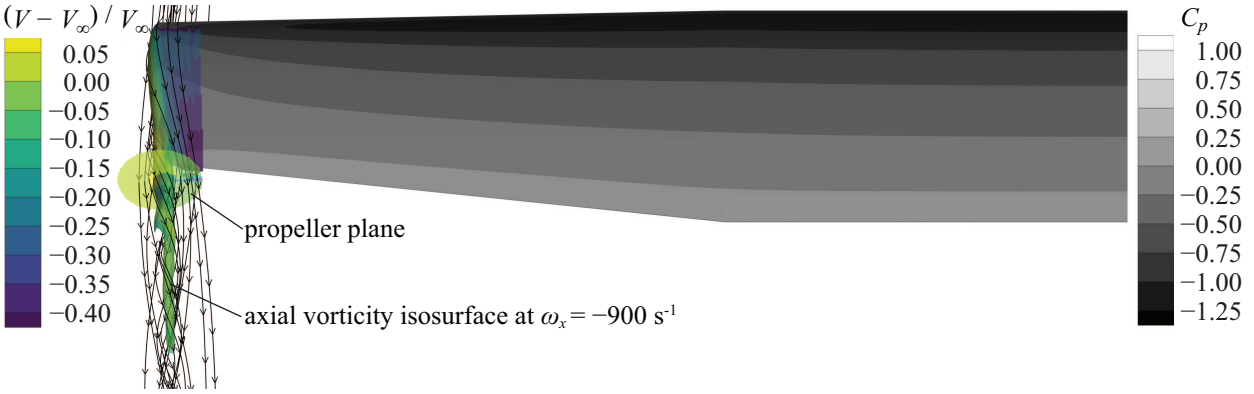

Fig. 4 Visualisation of wingtip flowfield and pressure coefficient distribution on the wing surface.

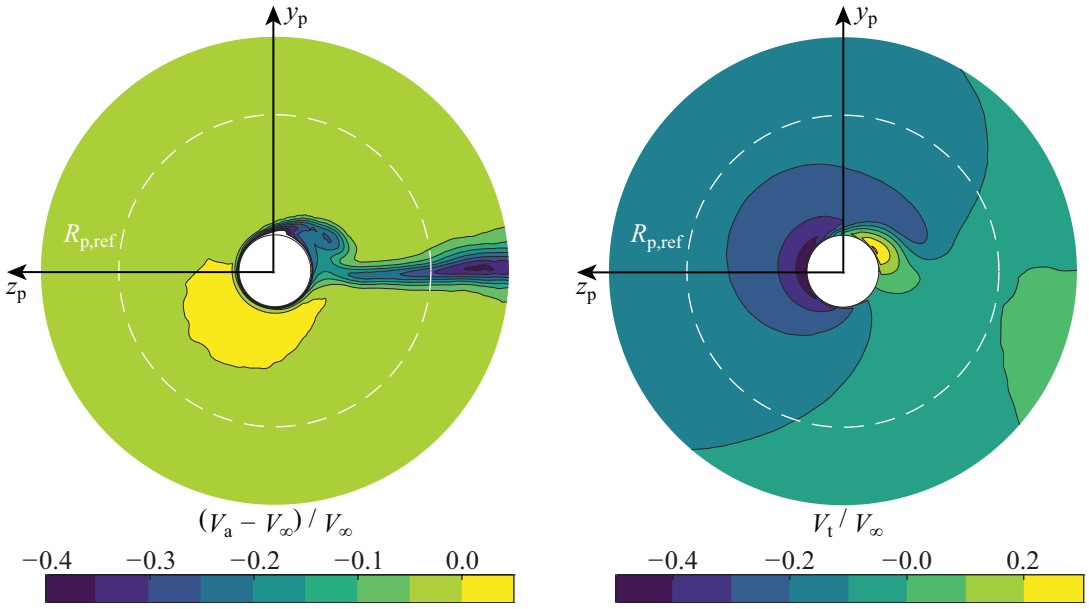

Fig. 5 Contour plots of axial and tangential velocity components at the propeller plane behind the left wingtip. The dashed line shows the propeller disc area for the reference XPROP propeller.

The resulting propeller designs for this flowfield are presented in Section V and the consequence of circumferential averaging will be further discussed in Section VII.

IV. Isolated Propeller Analysis

To establish confidence in PROPR, two comparisons were made. The first was with in-house windtunnel data of the XPROP propeller in uniform flow. In Fig. 6 a comparison is presented of the thrust and torque coefficient versus advance ratio for V_∞ = 30 m/s. Although at high advance ratios a significant deviation starts to appear for both thrust and torque coefficient, in the region of interest where C_T is higher, the match with the experimental data is satisfactory.

The second comparison was made with a CFD model of the isolated propeller from Ref. [13]. In Fig. 7 the thrust and torque distribution over a propeller blade are plotted for both PROPR and the CFD model for V_∞ = 30 m/s and an advance ratio of J = 0.74. This corresponds to a thrust of 16% of the isolated wing drag. The integrated loading is overestimated by PROPR with 4.5% and 7.6% in thrust and torque respectively. The shape of the thrust and torque distribution from PROPR and the CFD model are very similar except for at the tip of the blade. The local rise in thrust and torque in the CFD model due to the tip vortex is not captured in the PROPR results because of the single lifting line representation of the blade. Considering that in these comparisons acceptable agreement was found, a design study was performed with PROPR. This is presented in the next Section V.

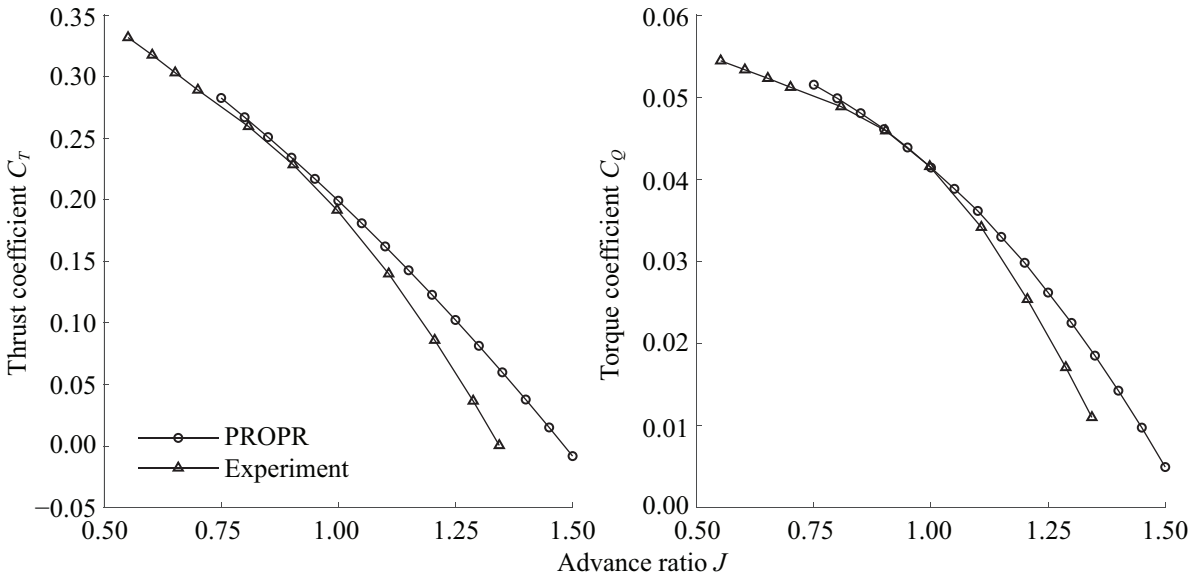

Fig. 6 Propeller performance from PROPR and inhouse windtunnel test for V_∞ = 30 m/s and $\beta_{0.7R_p}$ = 30°.

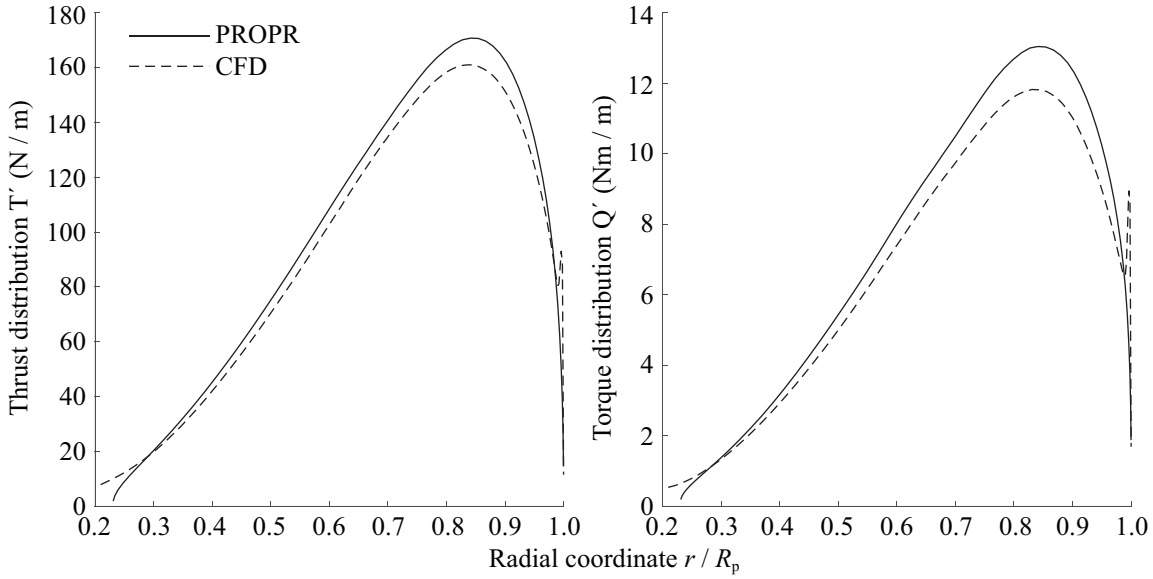

Fig. 7 Blade loading distributions from PROPR and CFD model for V_∞ = 30 m/s, $\beta_{0.7R_p}$ = 30° and J = 0.74.

V. Propeller Design Study

In this section the design optimization results from PROPR for a propeller placed in the wingtip flowfield are discussed. The different propeller designs are given in Table 4. The original XPROP propeller was tested in isolated and installed condition. The XPROP propeller was also optimized for minimum power in terms of blade pitch distribution and chord distribution, keeping the airfoil sections the same. This was done for isolated and installed conditions, denoted isoOpt and insOpt respectively. The former was tested both in isolated and installed conditions, while the latter was only tested in installed conditions. Note that these optimizations were performed for each thrust level separately and that for each thrust level the performance is given for optimum operating conditions in terms of $\beta_{0.7R_p}$ and J.

Table 4 Overview of different propeller geometries used in design study.

Propeller name	Description
XPROP-iso	Original XPROP propeller operating in isolated condition
isoOpt-iso	Optimized for isolated condition, operating in isolated condition
XPROP-ins	Original XPROP propeller operating in installed condition
isoOpt-ins	Optimized for isolated condition, operating in installed condition
insOpt-ins	Optimized for installed condition, operating in installed condition

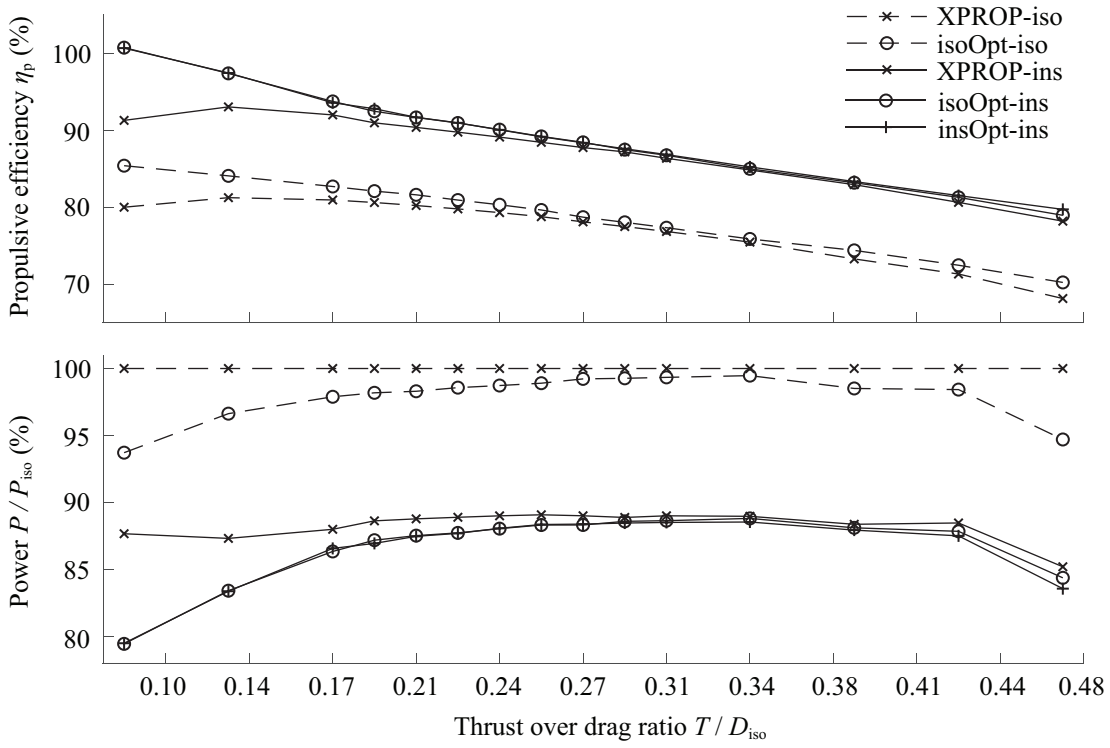

Fig. 8 Propeller optimization results showing the propulsive efficiency and power versus the thrust to wing drag ratio at constant radius $\mathbf{R_p/R_{p,ref}} = \mathbf{1.00}$ for isolated and installed conditions.

A. Propeller Optimization for Constant Radius

First, a design sweep was performed for a range of thrust levels, keeping the propeller radius equal to that of the original XPROP propeller $R_{p,ref}$. In Fig. 8 the propeller performance is shown for a range of design thrust levels with respect to the isolated wing drag T/D_{iso}. The propulsive efficiency $\eta_p = TV_\infty/P$ is plotted, as well as the relative power required with respect to the XPROP-iso propeller P/P_{iso}. Dashed lines refer to performance in isolated conditions, solid lines indicate installed propeller performance. Put in perspective, the wing induced drag is about 40% of the total wing drag in this condition, so a range of thrust levels is plotted from 25% up to 115% of the wing induced drag.

A number of trends can clearly be observed: The propulsive efficiency decreases with increasing design thrust in both the isolated and installed cases. This is expected since the propeller radius was kept constant. The possible efficiency gains due to installation and optimisation of the propeller are significant. Comparing insOpt-ins with XPROP-iso results, up to 20% increase in efficiency is achieved at lower design thrust levels by the combined effect of optimisation and installation, decreasing to approximately 10% and remaining constant at higher thrust levels. Although a more fair comparison is that of the insOpt-ins with the isoOpt-iso propeller, both optimised for their respective flowfield. Then, an efficiency increase up to 15% remains at the lowest thrust level, decreasing to 9% at the highest thrust level.

Looking at the power plot, the effectiveness of geometrical optimization in both isolated and installed conditions at low and high thrust levels is clearly visible. This effect diminishes at more average thrust levels, as the XPROP propeller is apparently designed for those thrust levels. The reduction in required power is significant when installing the propeller, even for the XPROP with non-optimized geometry. Reductions up to 20% are achieved when comparing insOpt-ins with XPROP-iso results, although looking at the most fair comparison with the isoOpt-iso propeller, a bit lower maximum power reduction of up to 15% is found. Note that the installed propeller with optimized geometry for isolated conditions (isoOpt) yields almost identical power reductions compared to the installed propeller with optimized geometry for installed conditions (insOpt). Thus, effectively the propeller geometry is optimized for the required thrust level and to a lesser degree for the non-uniformity in the flowfield. Only at the very high design thrust levels of $T/D_{\text{iso}} \geq 0.42$ a noticeable difference in performance between the two different optimized propellers is observed.

With increasing thrust, the power reduction due to installation converges quickly to a nearly constant value, meaning that the effective power reduction that can be achieved by installation of the propeller almost does not change with thrust requirement. One would expect that the effective power reduction would decrease with increasing propeller design thrust, as there is only a finite amount of energy to be 'extracted' from the wingtip flowfield present in the installed case. Because of the limited maximum thrust that can be delivered by the XPROP propeller it is not possible to investigate the effective power decrease at even higher thrust levels for the current propeller radius. The experimental work done by Patterson et al. [4] gives already an indication of the power reduction found at higher thrust levels, considering that the size of that propeller and its thrust relative to the wing was much larger. At similar lift coefficient the power reduction was found to be 14%, although this was for a non-optimized propeller design. Considering that this is of similar order to what was found in this study thus far, it may be that over a larger thrust range this relative power reduction stays more or less constant. To confirm this, in Section V.C the higher thrust regime up to a thrust equal to the cruise drag of the wing will be investigated with larger radius propellers.

B. Blade Loading and Geometry Changes Due to Optimization

The resulting changes in the propeller blade loading and geometry due to optimization and installation are discussed for two different design thrust levels: $T = 0.21D_{\text{iso}}$ and $T = 0.39D_{\text{iso}}$. First, the results from optimization of the XPROP propeller with $T = 0.21D_{\text{iso}}$ are discussed. In Fig. 9 the blade pitch angles, chord fractions, the profile efficiency and thrust distribution over the entire blade radius are shown. It is seen that the chord distribution of the insOpt and isoOpt propellers are nearly identical, even though the insOpt propeller was subjected to the non-uniform wingtip flowfield during optimization. In both cases, the chord lengths were reduced by as much as 40% compared to the XPROP propeller. A slight increase in blade pitch angle in the root sections is observed. Both the optimized isoOpt and insOpt propellers show significantly higher efficiency in the root sections. Presence of the non-uniform inflow enables further efficiency gains. Combined, this leads to a higher local profile efficiency for the insOpt propeller, especially for the root sections ($r/R_{\text{p}} < 0.4$). A clear trend is visible in the thrust distribution over the blade. Geometry optimization of the XPROP propeller causes the thrust distribution to shift inboard towards the root. Furthermore, the maximum value decreases. The same behavior to an even greater extent is observed when investigating the insOpt propeller. The combination of higher profile efficiency and the production of thrust there where the profile efficiency is higher makes this the most efficient propeller of the three.

Second, the optimization results with $T = 0.39D_{\text{iso}}$ are discussed. In Fig. 10 it is seen that the local blade chord lengths are increased in both the isoOpt and insOpt propeller designs compared to the original XPROP propeller. This geometry change due to optimization shows a reverse trend than what was seen for the lower design thrust in Fig. 9, where the chord fractions were decreased due to optimization. The local blade pitch angle is higher for both the isoOpt and insOpt propeller design, as was the case for the propellers optimized for $T = 0.21D_{\text{iso}}$. Also the improvements in local efficiency are similar, except for at the tip. Note that the efficiency of the XPROP propeller is relatively low in the tip region ($r/R_{\text{p}} > 0.85$) due to tip stall. Optimization of the propeller geometry reduces this tip stall and the overall efficiency distribution is again an almost ideal constant distribution. Finally, again an inboard shift in thrust distribution is observed for the optimized propeller geometries.

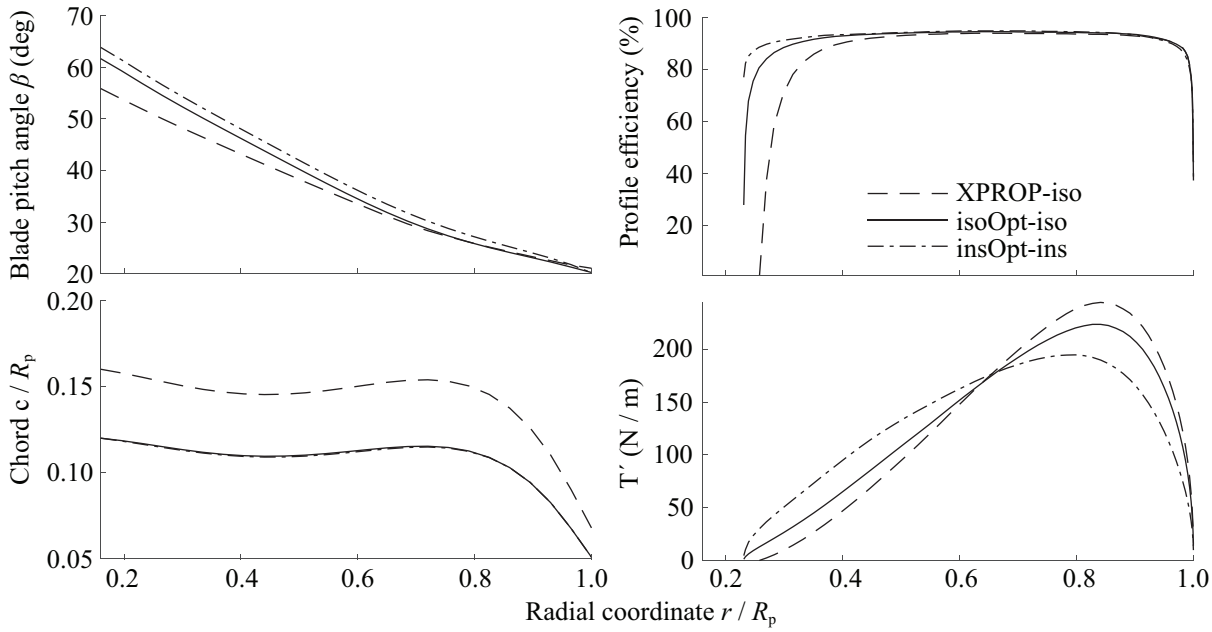

Fig. 9 Propeller blade loading and geometry changes due to optimization for T = 0.21D_{iso}.

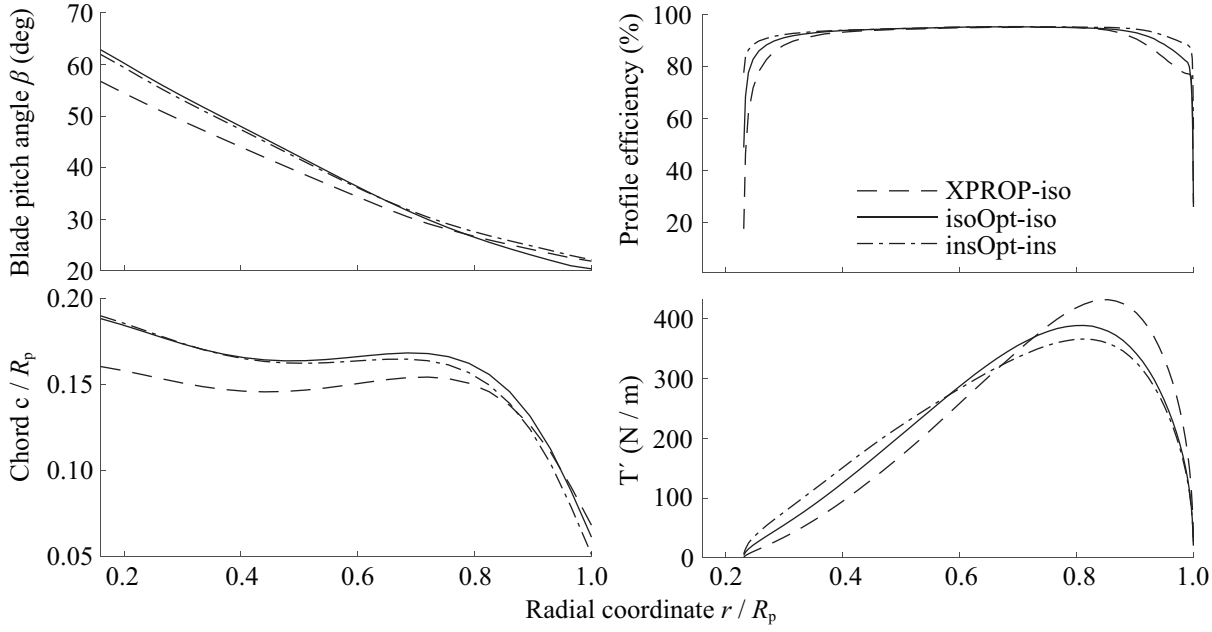

Fig. 10 Propeller blade loading and geometry changes due to optimization for T = 0.39D_{iso}.

C. Propeller Optimization with Varying Radius

The performance of the propeller placed in the wingtip flowfield was also investigated for propeller radii different from the XPROP propeller. The radius was varied between $0.75 - 1.50R_{\mathrm{p,ref}}$, where $R_{\mathrm{p,ref}}$ is the radius of the XPROP propeller. A design thrust range up to $T = D_{\mathrm{iso}}$ was analysed for the largest radius propeller. The hub dimension was kept constant and was not scaled with propeller radius. In this analysis the performance of the propeller optimized for installed condition and operating in installed condition, insOpt-ins, was compared to a propeller of equal radius optimized for isolated condition operating in isolated condition, isoOpt-iso. This is the most fair comparison since both propellers are optimised for their respective flowfield. The propeller performance results are given in Fig. 11 as a function of thrust level. For any given thrust level, the propulsive efficiency η_{p} increases with increasing propeller radius for all propeller designs. This is a straight forward result since, with increasing radius and equal thrust, more mass is accelerated by the propeller but with a lower velocity increase. The corresponding advance ratio is also higher for larger radii propellers due to the large reduction in required rotational speed n.

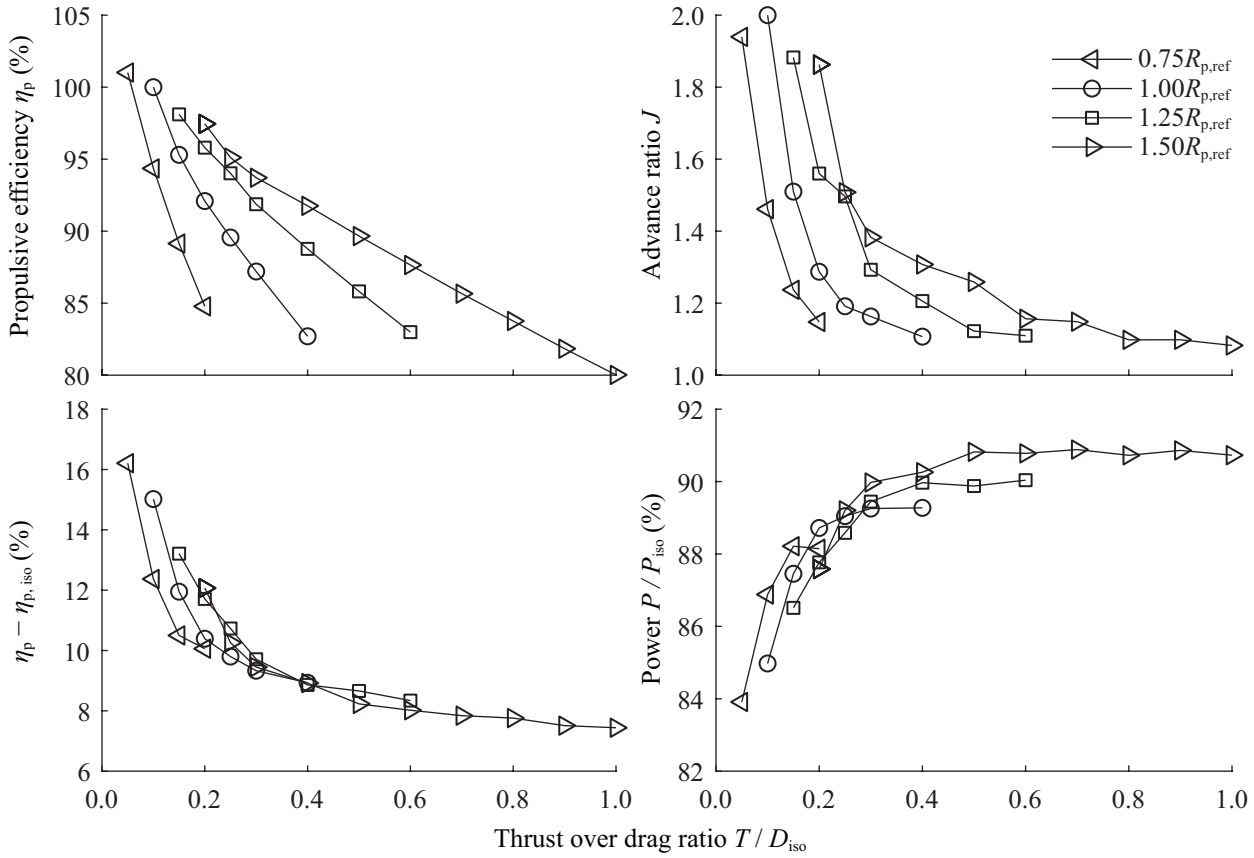

Fig. 11 Optimization results with varying propeller radius for installed condition with insOpt-ins design compared to isolated condition with isoOpt-iso design.

The gain in efficiency by installation of the propeller at the wingtip, $\eta_{\mathrm{p}} - \eta_{\mathrm{p,iso}}$, varies less with propeller radius. Only for low thrust levels of less than 30% of the wing drag, significant differences occur in the efficiency gain. While the efficiency gain decreases with thrust level, it does so at a reducing rate, decreasing to a still significant gain of 7.5% when the thrust equals the wing drag $T = 1.00D_{\mathrm{iso}}$. As discussed earlier for the optimisation results at equal radius, the power ratio P/P_{iso} seems to level off to an approximately constant value at larger thrust levels. This is also happening for the other propeller radii, however the relative power reduction reduces for larger propeller radii, reducing to a 9% reduction due to the wingtip flowfield for $1.50R_{\mathrm{p}}$.

VI. Actuator Disk–Wing Analysis

The upstream effect of the propeller designs on the wing performance was analyzed through CFD analyses of the wing with an actuator disk representation of the propeller. These simulations are of similar computational cost as the isolated wing simulations but do provide the required time-averaged upstream effect of the propeller at much reduced computational cost compared to the fully resolved propeller–wing simulation in Section VII. In Fig. 12 the wing lift coefficient C_L and lift-over-drag ratio L/D are plotted as a function of propeller thrust for a number of cases with varying propeller radius from Fig. 11. Results are also shown for the isolated wing.

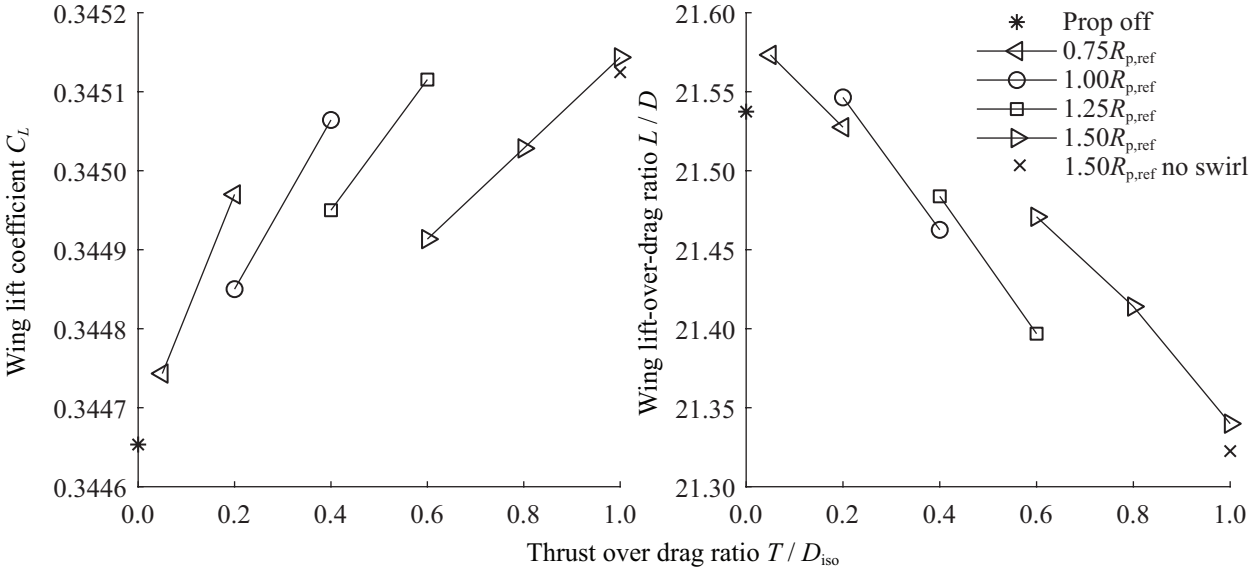

Fig. 12 Wing performance as function of propeller thrust investigated with an actuator disk.

The changes in wing lift coefficient due to propeller thrust are quite small and are only just larger than the estimated discretization uncertainty given in Table 3. Despite this, an increasing trend in C_L is visible with increasing propeller thrust level. This could be explained by a slightly stronger suction over the wing due to the presence of the propeller. Contrary to the lift coefficient, the lift-over-drag ratio decreases with increasing propeller thrust. Apparently the propeller slightly reduces the wing efficiency. Another observation is that with increasing propeller radius, the upstream effects of the propeller on the wing reduce. For the $1.50R_{\text{p}}$ case an additional simulation was performed where no swirl component was introduced by the actuator disk, denoted *no swirl*. It shows that the swirl component has only a minor impact on the wing loading. Thus, the reduction of swirl in the wingtip flowfield due to the propeller does not cause a significant change in wing loading and the observed changes are mainly an effect of the axial velocity increase. However in general, it is concluded that the upstream effect of the propeller on the wing loading is very limited for the investigated thrust range. A closer look at the downstream interaction of the wing on the propeller is presented in the next section.

VII. Propeller–Wing Analysis

To check the accuracy of PROPR for the non-uniform wingtip flowfield, and to investigate the unsteady behaviour of a wingtip-mounted pusher propeller, a fully resolved propeller–wing CFD simulation was performed. The original XPROP propeller was simulated installed on the wingtip at optimum operating condition in terms of $\beta_{0.7R_{\text{p}}}$ and J at a thrust of $T = 0.30D_{\text{iso}}$.

In Fig. 13 a the normalized blade thrust and torque as function of blade phase angle are shown, as defined in Fig. 14 b. In addition, the mean of the thrust and torque obtained from the transient CFD simulation are shown, as well as the thrust and torque values calculated using PROPR. As expected, the blade thrust and torque vary considerably over a rotation due to the circumferential non-uniformities in the flowfield that were shown in Fig. 5. Following the trajectory of the blade, clear trends are observed:

- $\varphi = 0°$: Initial position, blade pointing up and perpendicular to the wing surface.
- $\varphi = 90°$: Blade is fully outboard and subjected to the largest negative tangential velocities, thus highest thrust.

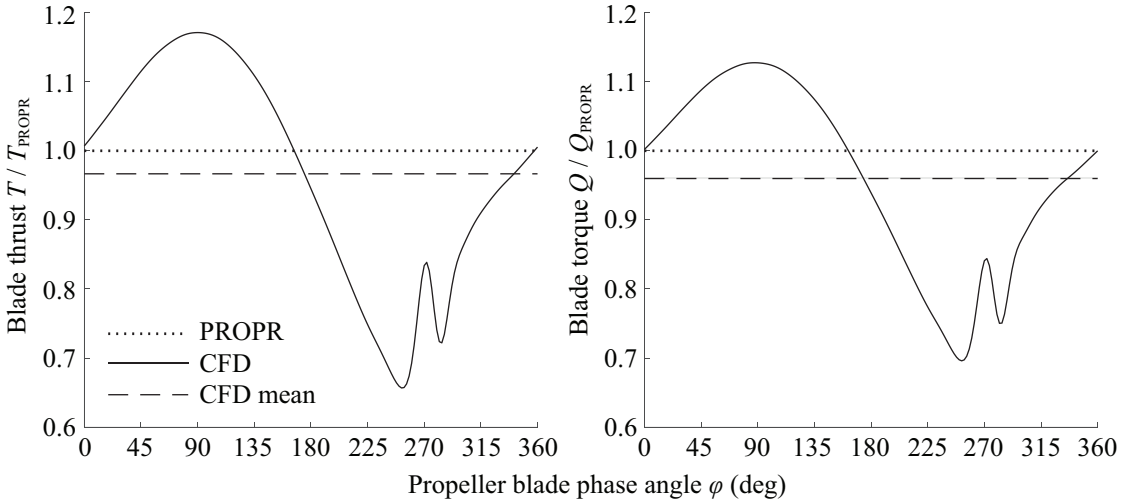

Fig. 13 Installed XPROP propeller blade thrust and torque evolution over a complete rotation for T = 0.30D$_{\mathrm{iso}}$.

- $\varphi = 180°$: Blade is again perpendicular to the wing but now pointing down. Thrust delivered with inflow from under the wing is slightly lower.
- $\varphi = 270°$: At this angle the blade is fully immersed in the wake region of the wing, showing a clear local peak in thrust, due to the lower axial velocity. This causes an increased angle of attack of the blade sections.

Identical trends are observed when investigating the torque evolution. The difference in mean thrust and torque obtained between CFD and PROPR are very similar to those obtained for the isolated propeller in Section IV. The blade thrust and torque are overestimated 3.3% and 4.0% by PROPR respectively. This provides confidence in the validity of PROPR given these non-uniform flowfields.

To get some more insight in the blade loading evolution, in Fig. 14 a the propeller blade thrust distribution is plotted at various blade positions as defined in Fig. 14 b. The blade distribution from PROPR is also shown. It is seen that the thrust distribution over the blade from PROPR is nearly identical to that found in the transient CFD simulation over blade 1. Blade 2 and 3 are subjected to the largest tangential velocity field and indeed show the highest thrust. Most notably, these blades experience a significantly higher thrust at the root sections of the blade. Blade 5 experiences the lowest blade loading because, as was shown in Fig. 5, the tangential velocity field at this location is near zero. A drop in thrust near the root occurring over blade 6 is seen, because it is immersed in a flowfield with locally positive tangential velocity. Blade 6 experiences this positive tangential velocity near the root, because it crosses the tip vortex of the wing. This becomes clear from Fig 15, where a tangential and an axial vorticity isosurface is shown at such levels that they identify the propeller blade tip vortices and wingtip vortex respectively. The propeller blades are at the same position as in Fig. 14 b. It is clear that blade 6 is starting to cross the wingtip vortex.

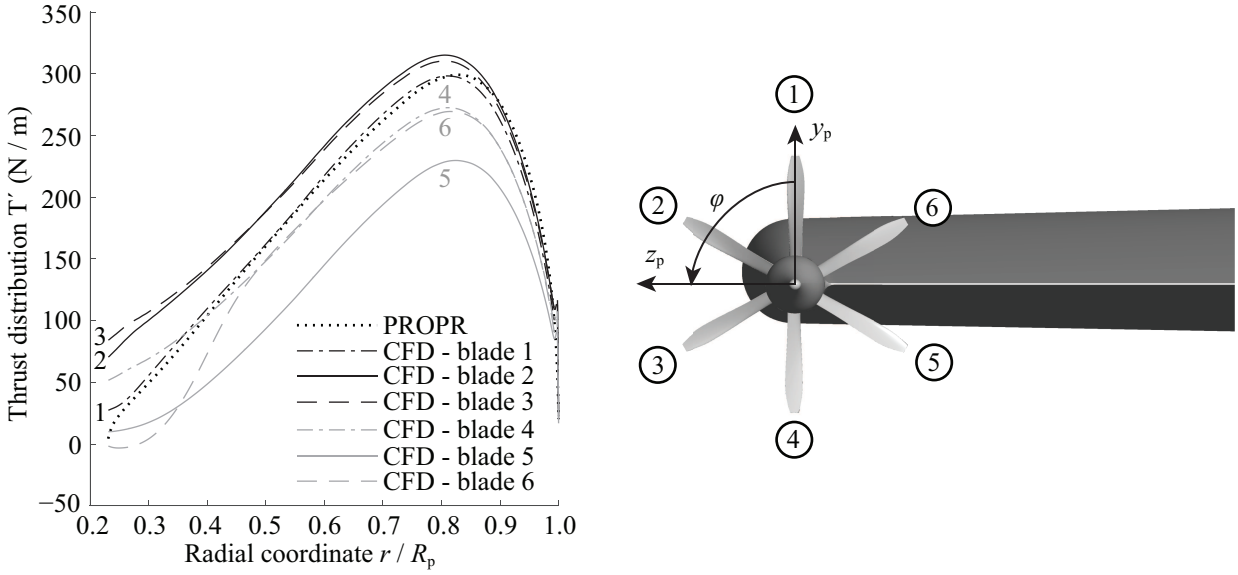

a) Propeller blade thrust distribution comparison. **b) Definition of blade positions.**

Fig. 14 Comparison of XPROP propeller blade thrust distributions at different blade positions for T = 0.30D$_{iso}$.

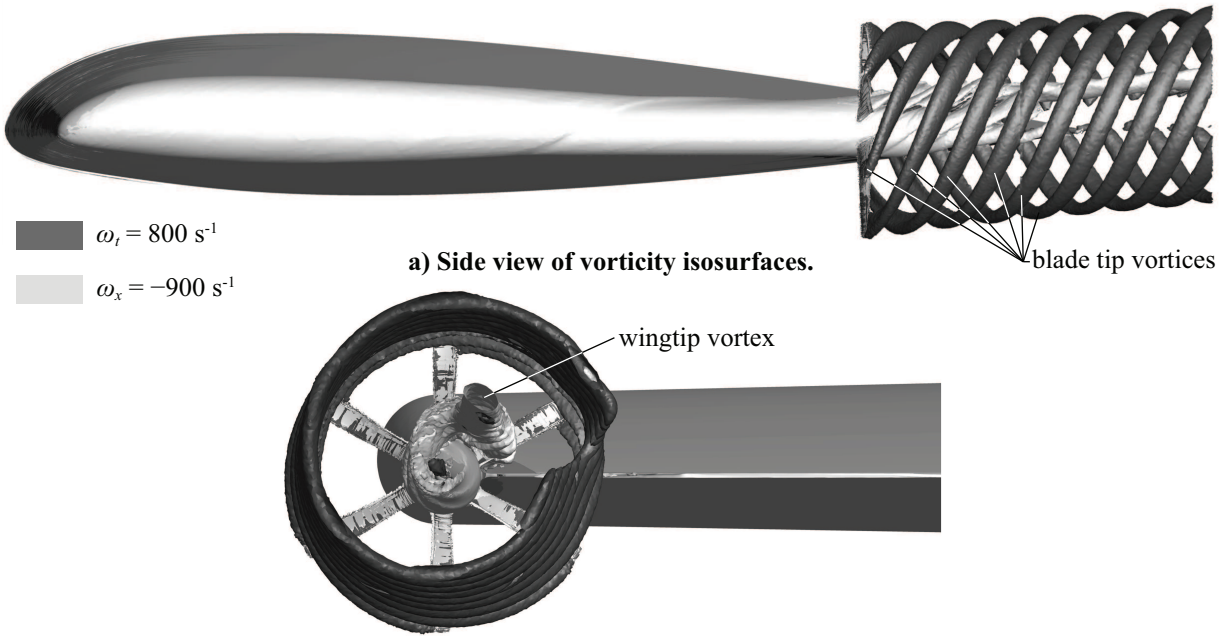

a) Side view of vorticity isosurfaces.

b) Rear view of vorticity isosurfaces.

Fig. 15 Vorticity isosurfaces identifying the XPROP propeller blade tip vortices and wingtip vortex.

VIII. Conclusions

A design framework for wingtip-mounted pusher propellers was established and verified with RANS CFD simulations. It was found that the following approach is valid: First a wingtip flowfield was extracted from an isolated wing simulation. Then, this flowfield was circumferentially averaged and used in a validated lifting-line based propeller analysis and optimisation routine named PROPR for aerodynamic design optimization. The upstream effect of the propeller on the wing performance was investigated with an actuator disk representation of the propeller in multiple wing simulations and was found to be very limited for the tested thrust levels. This was a requirement for the taken approach. However, a trend of increasing wing lift coefficient and decreasing lift-over-drag ratio was observed with increasing propeller thrust, which may become significant for higher thrust levels than currently investigated. At last, the resulting propeller performance from PROPR was in line with time-averaged propeller loading of fully resolved propeller-wing RANS CFD simulations, providing confidence in the validity of the approach. This was despite the large fluctuation found in the transient propeller blade loading due to circumferential non-uniformities in the inflow field.

With this design framework for wingtip-mounted pusher propellers, various conclusions on propeller design for wingtip-mounted pusher propellers are drawn:

- The possible propulsive efficiency gains for the propeller due to installation are significant: Up to 16% increase in efficiency was achieved at the lowest investigated thrust level of 5% of the wing drag, decreasing with a reducing slope to approximately 7.5% for the highest investigated thrust level of 100% of the wing drag.
- The propulsive efficiency gain was only significantly dependent on the propeller radius for low thrust levels of less than 30% of the wing drag.
- It was found that effectively the propeller geometry is optimized for the required thrust level and to a lesser degree for the non-uniformity in the flowfield.
- Propeller blade optimization and installation result in higher profile efficiency in the blade root sections and a more inboard thrust distribution over the blade.

Considering the propulsive efficiency benefits found in this study, wingtip-mounted pusher-propellers should be considered for (hybrid)-electric concepts. The propeller thrust should then be a design variable, determining together with the wing lift the resulting efficiency benefit from this aerodynamic interaction.

References

[1] Loth, J. L., and Loth, F., "Induced Drag Reduction with Wing Tip Mounted Propellers," *2nd Applied Aerodynamics Conference*, AIAA Paper 1984-2149, Aug. 1984. doi:10.2514/6.1984-2149.

[2] Miranda, L. R., and Brennan, J. E., "Aerodynamic Effects of Wingtip-Mounted Propellers and Turbines," *4th Applied Aerodynamics Conference*, AIAA Paper 1986-1802, June 1986. doi:10.2514/6.1986-1802.

[3] Sinnige, T., van Arnhem, N., Stokkermans, T. C. A., Eitelberg, G., and Veldhuis, L. L. M., "Wingtip-Mounted Propellers: Aerodynamic Analysis of Interaction Effects and Comparison with Conventional Layout," *Journal of Aircraft*, Vol. 56, No. 1, 2019, pp. 295–312. doi:10.2514/1.C034978.

[4] Patterson Jr, J. C., and Bartlett, G. R., "Effect of a Wing Tip-Mounted Pusher Turboprop on the Aerodynamic Characteristics of a Semi-Span Wing," *AIAA/SAE/ASME/ASEE 21st Joint Propulsion Conference*, AIAA Paper 1985-1286, July 1985. doi:10.2514/6.1985-1286.

[5] Janus, J. M., Chatterjee, A., and Cave, C., "Computational Analysis of a Wingtip-Mounted Pusher Turboprop," *Journal of Aircraft*, Vol. 33, No. 2, 1996, pp. 441–444. doi:10.2514/3.46959.

[6] Stokkermans, T., Voskuijl, M., Veldhuis, L., Soemarwoto, B., Fukari, R., and Eglin, P., "Aerodynamic Installation Effects of Lateral Rotors on a Novel Compound Helicopter Configuration," *AHS International 74th Annual Forum & Technology Display*, May 2018.

[7] Moore, M. D., and Fredericks, B., "Misconceptions of Electric Propulsion Aircraft and their Emergent Aviation Markets," *52nd Aerospace Sciences Meeting*, AIAA Paper 2014-0535, Jan. 2014. doi:10.2514/6.2014-0535.

[8] Borer, N. K., Patterson, M. D., Viken, J. K., Moore, M. D., Clarke, S., Redifer, M. E., Christie, R. J., Stoll, A. M., Dubois, A., Bevirt, J., Gibson, A. R., Foster, T. J., and Osterkamp, P. G., "Design and Performance of the NASA SCEPTOR Distributed Electric Propulsion Flight Demonstrator," *16th AIAA Aviation Technology, Integration, and Operations Conference*, AIAA Paper 2016-3920, June 2016. doi:10.2514/6.2016-3920.

[9] Stokkermans, T. C. A., van Arnhem, N., and Veldhuis, L. L. M., "Mitigation of Propeller Kinetic Energy Losses with Boundary Layer Ingestion and Swirl Recovery Vanes," *Proceedings of the 2016 Applied Aerodynamics Research Conference*, Royal Aeronautical Soc., London, 2016, pp. 56–69.

[10] Nootebos, S., "Aerodynamic Analysis and Optimisation of Wingtip-Mounted Pusher Propellers," Master's thesis, Delft University of Technology, 2018.

[11] Costruzioni Aeronautiche TECNAM S.p.A., "P2012 Traveller," https://www.tecnam.com/aircraft/p2012-traveller/, Accessed: 2018-10-30.
[12] Alba, C., "A Surrogate-Based Multi-Disciplinary Design Optimization Framework Exploiting Wing-Propeller Interaction," Master's thesis, Delft University of Technology, 2017.
[13] Stokkermans, T. C. A., and Veldhuis, L. L. M., "Propeller Performance at Large Incidence Angle for Compound Helicopters and eVTOL," (unpublished).
[14] Anon., "ANSYS® Academic Research Release 18.1 Help System, Fluent," ANSYS, inc., Canonsburg, PA, 2017.
[15] Barth, T. J., and Jesperson, D. C., "The Design and Application of Upwind Schemes on Unstructured Meshes," *27th Aerospace Sciences Meeting*, AIAA Paper 1989-366, Jan. 1989. doi:10.2514/6.1989-366.
[16] Kim, S.-E., and Rhee, S. H., "Efficient Engineering Prediction of Turbulent Wing Tip Vortex Flows," *Computer Modeling in Engineering & Sciences (CMES)*, Vol. 62, No. 3, 2010, pp. 291–309. doi:10.3970/cmes.2010.062.291.
[17] Spalart, P. R., and Allmaras, S. R., "A One-Equation Turbulence Model for Aerodynamic Flows," *30th Aerospace Sciences Meeting and Exhibit*, AIAA Paper 1992-439, June 1992. doi:10.2514/6.1992-439.
[18] Dacles-Mariani, J., Zilliac, G. G., Chow, J. S., and Bradshaw, P., "Numerical/Experimental Study of a Wingtip Vortex in the Near Field," *AIAA Journal*, Vol. 33, No. 9, 1995, pp. 1561–1568. doi:10.2514/3.12826.
[19] Spalart, P. R., and Rumsey, C. L., "Effective Inflow Conditions for Turbulence Models in Aerodynamic Calculations," *AIAA Journal*, Vol. 45, No. 10, 2007, pp. 2544–2553. doi:10.2514/1.29373.
[20] Stokkermans, T. C. A., van Arnhem, N., Sinnige, T., and Veldhuis, L. L. M., "Validation and Comparison of RANS Propeller Modeling Methods for Tip-Mounted Applications," *AIAA Journal*, Vol. 57, No. 2, 2019, pp. 566–580. doi:10.2514/1.J057398.
[21] Drela, M., and Youngren, H., "XROTOR 7.55 (Computer software)," , Retrieved from: http://web.mit.edu/drela/Public/web/xrotor/.
[22] Hirner, A., Dorn, F., Lutz, T., and Krämer, E., "Improvement of Propulsive Efficiency by Dedicated Stern Thruster Design," *7th ATIO Conference*, AIAA Paper 2007-7702, Sept. 2007. doi:10.2514/6.2007-7702.
[23] Sinnige, T., "The Effects of Pylon Blowing on Pusher Propeller Performance and Noise Emissions," Master's thesis, Delft University of Technology, 2013.
[24] Borer, N., and Moore, M., "Integrated Propeller - Wing Design Exploration for Distributed Propulsion Concepts," *53rd AIAA Aerospace Sciences Meeting*, AIAA Paper 2015-1672, Jan. 2015. doi:10.2514/6.2015-1672.
[25] Humpert, B. J., Gaeta, R. J., and Jacob, J. D., "Optimal Propeller Design for Quiet Aircraft Using Numerical Analysis," *21st AIAA/CEAS Aeroacoustics Conference*, AIAA Paper 2015-2360, June 2015. doi:10.2514/6.2015-2360.
[26] Drela, M., "XFOIL: An Analysis and Design System for Low Reynolds Number Airfoils," *Low Reynolds Number Aerodynamics*, Springer Berlin Heidelberg, 1989.
[27] Snel, H., Houwink, R., and Bosschers, J., "Sectional Prediction of Lift Coefficients on Rotating Wind Turbine Blades in Stall," Tech. Rep. ECN-C–93-052, Netherlands Energy Research Foundation, 1994.
[28] Roache, P. J., "Quantification of Uncertainty in Computational Fluid Dynamics," *Annual Review of Fluid Mechanics*, Vol. 29, No. 1, 1997, pp. 123–160. doi:10.1146/annurev.fluid.29.1.123.
[29] Eça, L., and Hoekstra, M., "Discretization Uncertainty Estimation Based on a Least Squares Version of the Grid Convergence Index," *Proceedings of the Second Workshop on CFD Uncertainty Analysis*, Oct. 2006.